Wire resonator as a broadband Huygens superscatterer

Dmytro Vovchuk [1,2,*,†] Sergei Kosulnikov [1,3,†] Roman E. Noskov [1,†] and Pavel Ginzburg[1,4]

[1]*Tel Aviv University, Ramat Aviv, Tel Aviv, 69978, Israel*
[2]*Department of Radio Engineering and Information Security, Yuriy Fedkovych Chernivtsi National University, Chernivtsi, 58012, Ukraine*
[3]*Department of Physics and Engineering, ITMO University, Saint Petersburg, 197101, Russia*
[4]*Center for Photonics and 2D Materials, Moscow Institute of Physics and Technology, Dolgoprudny, 141700, Russia*

Interference phenomena allow tailoring propagation of electromagnetic waves by controlling phases of several scattering channels. Huygens element, being a representative example of this approach, enables enhancement of the scattering from an object in a forward direction, while the reflection is suppressed. However, a typical resonant realization of Huygens element employs constructive interference between electric and magnetic dipolar resonances that makes it relatively narrowband. Here we develop the concept of a broadband resonant Huygens element, based on a circular array of vertically aligned near-field coupled metal wires. Accurate management of multipole interference in an electrically small structure results in directional scattering over a large bandwidth, acceding 10% of the carrier frequency. Being constructed from nonmagnetic materials, this structure demonstrates a strong magnetic response appearing in dominating magnetic multipoles over electric counterparts. Moreover, we predict and observe higher-order magnetic multipoles, including hexadecapole (M16-pole) and magnetic triakontadipole (M32-pole) with quality factors, approaching 6000. The experimental demonstration is performed at the low GHz spectral range. Broadband Huygens elements can be employed in a set of practical applications, where compact electromagnetic devices for tailoring wave propagation are needed, i.e., antenna devices, directional reflectors, and even solar cells, given that the concept is scaled to the optical frequency range.

I. INTRODUCTION

Increasing scattering efficiencies of subwavelength structures is a long-standing objective of applied electromagnetic theory. Quite a few fundamental bounds have been proposed and subsequently challenged with advanced designs. For example, the celebrated Chu-Harrington limit defines minimally achievable quality factors (Q factors) of subwavelength lossless resonators [1]. On another hand, it is relatively well known that the maximal scattering efficiency of a resonant subwavelength object does not depend on its size if internal material losses are neglected. In a single resonance case, a fundamental limit of scattering is $(2l' + 1)\lambda^2/(2\pi)$, where λ is the free space wavelength and l' is related to orbital angular momentum of a multipolar resonance ($l' = 1$ is the electric or magnetic dipolar case. Strictly speaking, this limit applies on geometries with a spherical symmetry). A vast majority of reported designs operates at dipolar resonances. In the case of lossless structures the upper dipolar bound is $3\lambda^2/(2\pi)$ [2–6].

While subwavelength structures can be quite efficient scatterers, the penalty of size reduction is a dramatic growth in the Q factor, described in a single resonance case by the Chu-Harrington bound. A strategy to bypath this limitation is to involve several spectrally overlapping multipolar resonances. This approach allows increasing the bandwidth while keeping strong scattering efficiency with help of cascading resonances.

The concept of multipolar spectral overlap has been developed in the field of electrically small antennas in order to increase directivity. The commonly accepted directivity bound is typically related to the antenna aperture (A) in units of the operational wavelength (λ) square as $G_{\max} = 4\pi A/\lambda^2$, meaning that high directivity cannot be obtained with small (nonresonant) apertures. However, the so-called Einstein's needle radiation (extremely high directivity) can be engineered in a small (even a deeply subwavelength) structure if a large number of multipoles interferes constructively [7]. Quite a few theoretical approaches to achieve high directivity and superscattering have been reported. For example, core-shell spherical or cylindrical geometries were extensively explored. Those structures, having closed form analytical solutions (i.e., Mie theory), are subject to fast optimization and, hence, were found to promise a significant overcome of classical bounds [8–12].

However, practical limitations significantly degrade the theoretical predictions [13]. In particular, employment of high-order multipoles in subwavelength geometries increases the stored near-field energy within a structure, giving rise to strong internal material losses. Another important issue is the fabrication tolerance. Any imperfection with respect to an original design shifts phases of multipoles and destroy their constructive interference. As an intermediate summary here, suggesting partial solutions to the beforehand mentioned challenges, is to avoid using lossy materials in the designs (e.g., printed circuit board (PCB) substrates) and employ geometrically simple elements to facilitate fabrication tolerances. Following these guidelines, we propose a set of

---
*Corresponding author: dimavovchuk@gmail.com
†These authors contributed equally to this work.

straight copper wires within a styrofoam host as a miniature superscatterer.

Another topic, closely related to the scattering management, is the emerging field of metasurfaces [14–23] which allow tailoring electromagnetic energy flow with subwavelength thin patterned layers. In a vast majority of the reported designs, resonant elements are organized within two-dimensional arrays, and collective interaction phenomena are obtained. One of them is the backscattering cancellation based on the interference of electric and magnetic dipoles in a single particle. This effect was first proposed by Kerker *et al.* [24], and since then the concept has been advanced and generalized in many realizations, e.g., Refs. [25–31]. Particles, which demonstrate a suppressed backward scattering, are also referred to as Huygens elements, as they might act as sources of secondary waves in Huygens-Fresnel diffraction theory. Being an interference phenomenon, *resonant* Huygens elements are inherently narrowband in a sharp contrast to a nonresonant case when electric and magnetic dipoles can constructively interfere in a broadband domain but with very low scattering efficiency [30,32]. It is worth noting that the challenge is to obtain a strong forward scattering and simultaneously suppress backward scattering. It is obvious that relaxing the first conditions makes the problem trivial; for example, vacuum is an ultimately broadband forward scatterer, but it does not provide any tuning capability and the scattering efficiency is identically zero.

Here we develop and experimentally demonstrate a concept of a *broadband resonant* Huygens element, implemented as a wire resonator. It is based on a circular array of wires, embedded in a styrofoam host. The resonator supports a variety of multipolar resonances, which emerge from a near-field coupling between short metal wires. First, we perform numerical analysis of the scattering efficiency as a function of the number of wires and find the optimal number of wires meeting a trade-off between simplicity and performance of the structure. Adjusting the number of wires and other geometrical parameters (wire's length and the array radius) enables us to obtain an efficient control over the multipolar response and cover a relatively large bandwidth with the overlapping resonances. Accurate control of amplitudes and phases allows achieving performances of a Huygens element.

The concept of a circular wire resonator should not be confused with circular antenna arrays, e.g., Refs. [33–35]. Interactions in those structures, being more than a wavelength in size, is governed by higher-order modes, which might provide superior antenna characteristics [35–37]. Our configuration, however, is smaller in size and its operation is described by spectrally overlapping lower order modes. As the result, broadband directional scattering can be achieved, as it will be shown hereinafter.

The manuscript is organized as follows: Sec. I shows a preliminary numerical analysis of the structure in order to obtain a set of optimal parameters, i.e., a number of wires in the array. Section II describes the eigenmodes of the resonator and their relation to the multipolar responses. Section III discusses far-field signatures of the modes, underlining their contributions to the interaction. Sections IV and V concentrate on an experimental verification and the broadband Huygens element operation.

II. THE STRUCTURE'S OPTIMIZATION

An array of near-field coupled vertical wires supports a variety of multipolar modes. For a relatively short wire (a standalone wire supports a single mode in the desired frequency range) and taking into account the mode degeneracy, the number of eigenmodes equals to $(N + 1)/2$ if N is odd or $N/2 + 1$ if N is even [33,38], where N is number of wires (here wire and azimuthal modes do not mix). In the case of long wires, however, the family of modes will be much broader, as different types of mixing will take place. Hence, it is quite appealing to increase the number of wires within an array to achieve a richer mode structure. Nevertheless, strong near-field coupling in the subwavelength geometry sets certain limitations and complexity, which manifest itself in mode hybridization. Here we will explore a circular array of short metal wires, equidistantly distributed on a cylindrical surface [Fig. 1(a)]. The first objective of the investigation aims in achieving a large scattering efficiency in a small structure that will surpass the Chu-Harrington limit (note, that under standard definitions the resulting structure only approaches be an electrically small). For this purpose, a numerical optimization, based on the finite element method is performed. The investigated geometry consists of a variable number of half-wavelength thin metal wires (perfect electric conductor is taken of the initial analysis), alighted on a cylinder with the radius $R = 33$ mm. The wire length is chosen to be 60.7 mm, corresponding to a dipole wire resonance around 2 GHz, which is the relevant frequency range from wireless communications perspectives. The structure is illuminated with a plane wave, propagating along the Z axis and polarized along the Y axis.

Figures 1(b) and 1(c) summarize the results, showing the scattering efficiency as a function of system's parameters. It is quite remarkable that the maximal efficiency approaches the value of 16.2. The not normalized scattering cross section is $650 \, \text{cm}^2$, while the single channel ($l' = 1$) limit is $(2l' + 1)\lambda^2/2\pi \approx 107 \, \text{cm}^2$ (at 2 GHz) is overcame by a factor of 6. This enhancement, however, saturates fast and can be obtained with an array of 5 five wires [Fig. 1(c)]. At the same time, the resonant frequency weakly depends on the number of wires and stays close to a dipole resonance of a single wire. As it will be shown hereinafter, mode hybridization (bonding and antibonding [39]) causes splitting around an initial resonant frequency.

In order to get an insight into physical phenomena of modes within circular wire resonators, an 11-wire structure [to ensure reaching the scattering efficiency plateau, Fig. 1(c)] will be investigated and the effect of strong scattering and broadband Huygens behavior will be revealed.

III. EIGENMODES OF A CIRCULAR WIRE RESONATOR

The optimized structure of 11 vertically aligned copper wires, equidistantly distributed over a cylindrical surface [Fig. 2(a)], will be investigated next. Experimental conditions correspond to the following values: wires' diameter and length are 1 and 60.7 mm, respectively, while the radius of the foam cylinder is 33 mm. Styrofoam, the transparent for GHz electromagnetic radiation, has been used to host metal wires (the
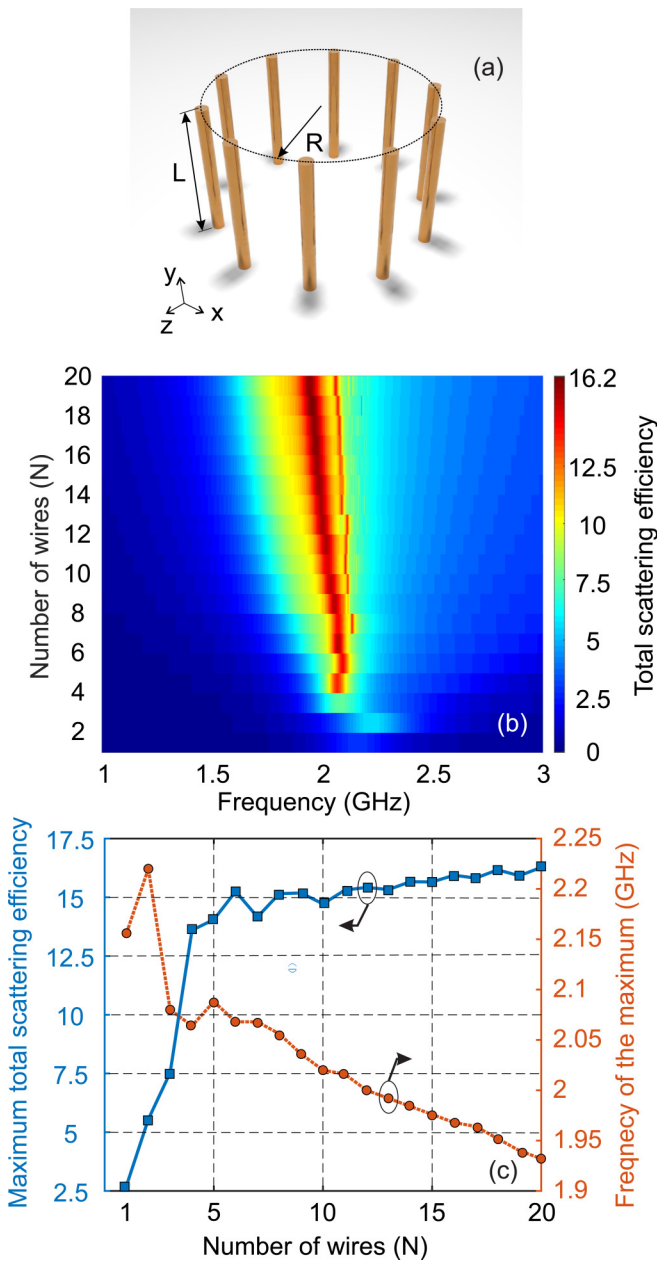
FIG. 1. (a) HERE Schematics of a circular wire array; a set of vertically aligned wires are equidistantly distributed on a cylinder's surface. (b), (c) Numerical analysis of the scattering efficiency (the values are normalized to the geometric cross section of the structure, $2R \times L$). Illumination, a plane wave, propagating along the Z axis and polarized along the Y axis. (b) The total scattering efficiency as a function of frequency and the number of wires within the array. (c) The maximum scattering efficiency (left) and the corresponding frequency (right) as functions of the number of wires (N). Black arrows link the data with relevant accesses.

wires were heated and squeezed into the foam to obtain more accurate location). Numerical and experimental investigations to reveal electromagnetic properties of the structure include near-to-near [Fig. 2(a)], near-to-far [Fig. 2(b)] and far-to-far [Fig. 2(c)] field excitation and measurement methods. The near-field excitation (Tx probe) and the receiving/scanning (Rx probe) are realized as magnetic field loop probes, located

near the sample surface. Setups for the far-field measurements include Tx and Rx horn antennas, allocated at the distance of 2.5 m from the sample to satisfy the Fraunhofer condition (horns are aligned along the wires to receive the proper polarization). The first configuration is needed to excite the entire modes of the structure (including dark weakly radiative ones) and to measure their field distributions. The second configuration detects the radiation efficiencies of the modes, while the last layout is the typical scattering scenario to test Huygens element performances.

In order to probe the entire modes of the structure (at the expected frequency range 1.8–2.6 GHz), the array is excited with a small nonresonant near field loop (Tx) and the complex reflection coefficient (S_{11} parameter) spectrum is acquired. An optimal (most efficient excitation of maximal number of modes) position of Tx with respect to the structure was found to be at the middle of one of the wires. The S_{11}-parameters spectra are presented in Fig. 3, which clearly show six high quality (high-Q) resonances.

Next, we scan near-field distributions at the relevant frequencies corresponding to the minima of S_{11} parameter (Fig. 4). Magnetic field probe (a loop) is placed at the distance of 2 mm from the cylinder and moved around the structure [Fig. 2(a)]. This circular scan is repeated for a different height of the probe, which maps the entire structure from the bottom to the top. The orientation of the probe allows detecting the azimuthal (within a good approximation) component of the magnetic field, including amplitude and phase. MiDAS system (ORBIT/FR Engineering Ltd.) is used to perform the experiment, while the sample is placed at the center of a rotating stage. Azimuthal locations of the wires correspond to the following angles: $\pm 18°$; $\pm 54°$; $\pm 90°$; $\pm 126°$, and $\pm 162°$. An additional wire is situated at $180°$, where Tx excitation probe is placed. The field scanning in the experiment is performed from $-170°$ to $+170°$. Scanning along the vertical axis is executed in the range from -40 to $+40$ mm to cover the entire geometry.

Eigenmodes of a circular array of omnidirectional scatterers (in-plane in our case) can be characterized by an azimuthal order, similarly to so-called phase-modes in circular antenna arrays [33–35]. According to Bloch theorem, phase variations of wire dipole moments obey geometrical periodicity of the structure as $p_n \sim \cos(2\pi \frac{n}{N} l)$, where l is the mode azimuthal order and n is the wire's ordinal number. Specifically, the 11-wire array possesses six eigenmodes.

Figure 4 and Table I summarize the results of the numerical eigenmode analysis, predictions of Bloch theorem, and the measurements. We underline a qualitative agreement between all these approaches. It is instructive to relate the classification by the azimuthal order to Cartesian multipoles [40]. In the lowest order mode ($l = 0$) there is no phase shift between wires that results in a dominating electric dipole (ED) response of the whole structure associated with strong scattering/radiation losses and a low Q factor. An increase in the azimuthal order gives rise to alternating polarity of currents, exited on wires, and nontrivially configured loops, which serve as sources of magnetic field, so that $l = 1$ corresponds to magnetic dipole (MD), $l = 2$ corresponds to the magnetic quadrupole (MQ), $l = 3$ to the magnetic octupole (MO), $l = 4$ to the magnetic hexadecapole (M16-pole), and
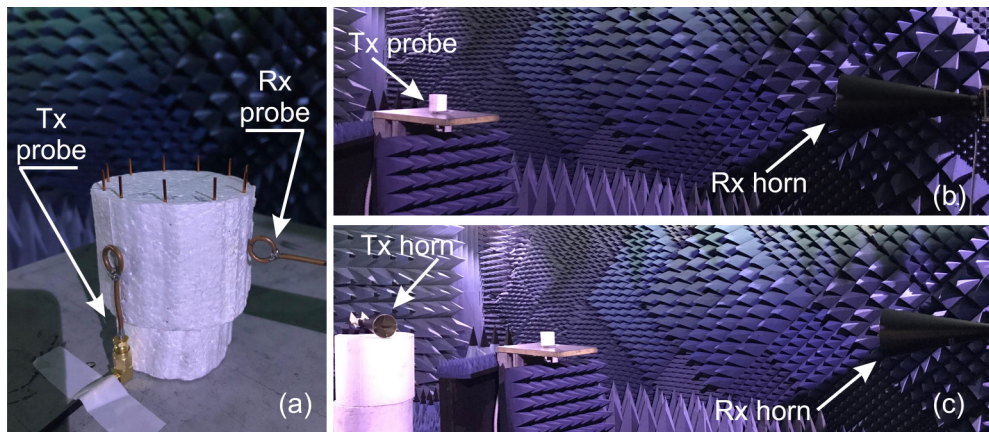
FIG. 2. Photographs of experimental setups in an anechoic chamber. The sample consists of $N = 11$ copper wires equidistantly distributed on a styrofoam cylinder's surface. Three types of setups are (a) near-field-to-near-field excitation (both Tx and Rx are realized with near-field magnetic loop probes); (b) near-field-to-far-field excitation (Tx is a near-field magnetic loop probe and Rx is a far-field horn); (c) far-field-to-far-field excitation (both Tx and Rx are realized as the far-field horn antennas).

$l = 5$ to the magnetic triakontadipole (M32-pole) (rigorous field decomposition with respect to Cartesian multipoles is presented in Fig. 6). A similar scenario has also been observed in circular arrays of metal nanoparticles, where collective plasmon resonances give rise to artificial magnetism at optical frequencies [41,42]. Importantly, the higher azimuthal order also leads to the higher Q factor as a result of stronger near field concentration and weaker scattering/radiation efficiency. In absence of Ohmic losses (or when those are negligible), scattering/radiation efficiency governs Q factors that are remarkably high for an open resonator in cases of $l = 4$ and $l = 5$.

The resonant frequencies and Q factors obtained in the experiment are fitted relatively well with the numerical modeling. Accurate retrieval of sharp resonances is quite challenging and, hence, numerical predictions deviate from the experiment, especially in the case of high-order multipoles (Table I). Experimental Q factors are extracted from the S_{11} spectrum, while the theoretical values are obtained from the eigenmode analysis. ED and MD modes, which are theoretically predicted, were not found in the experiment because of the relatively low Q factor (below 20). In this case, resonant peaks are mixed with tails of other nearby resonances.

Also, we note that the geometry of the real structure is not ideally symmetric. As a result, the modal degeneracy is removed, and the measurements show splitting of modes with $l = 4$ and $l = 5$ with slightly shifted resonant frequencies, while the Bloch theorem predicts a single mode per a single azimuthal order. This experimental aspect reflects the asymmetry in the realization and underlines the impact of fabrication tolerance on performances of highly resonant structures, as discussed in the introduction.

IV. FAR-FIELD SIGNATURES OF HIGH-ORDER MULTIPOLES

The next step is to estimate far-field signatures of the eigenmodes. It is worth noting that balancing those contributions will allow achieving broadband Huygens element, which will be discussed in the next section.

The experimental setup for far-field estimation is presented in Fig. 2(b). Here the sample is excited by the Tx near-field probe and the radiated patterns are acquired with the help of Rx horn antenna, located at the far-field region. Circular scan around the sample allows measuring the radiation in plane. Figure 5 shows far-field patterns (E field) along with the overall in plane radiated power spectra (more accurate analysis requires deconvoluting the radiation pattern of the receiving horn antenna from the measured data or performing a normalization to a tabulated object). Signatures of the eigenmodes can be clearly identified. For example, the four-lobes E-field structure (at 2.055 GHz) corresponds to the MQ eigenmode with $l = 2$. Other modes can be identified in a similar fashion, comparing Fig. 5 with Table I. Higher order modes have lower radiation efficiencies and, as a result, the far-field patterns are noisier (data in the insets to Fig. 5 is normalized to unity for each one independently).
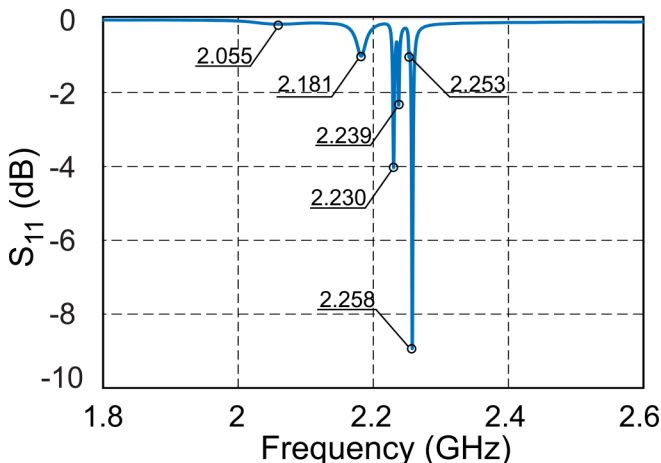

FIG. 3. The measured reflection coefficient [abs(S_{11}) in dB] spectrum. The excitation configuration appears in Fig. 2(a).
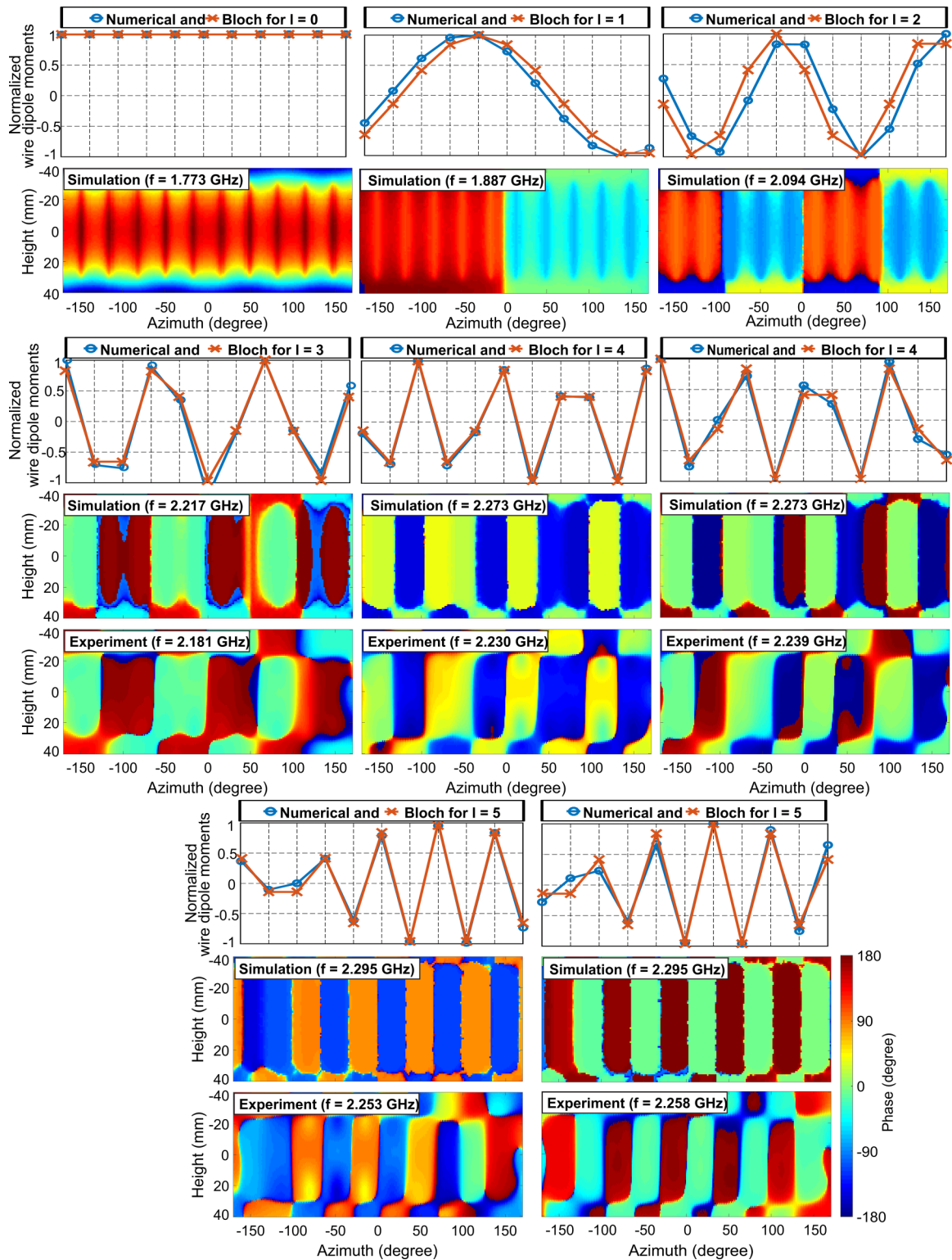
FIG. 4. Characterization of eigenmodes within a circular wire array: numerical simulations, near-field measurements, and Bloch theorem analysis. Experimental acquisition is performed with the near-field scan of azimuthal component of the magnetic field distributions [Fig. 2(a)]. Resonances of the modes and their classification appear in Table I. The eigenmodes with $l = 0$ and $l = 1$ have not been revealed in the experiment due to low Q factors. The mode with $l = 2$ appears in S_{11} but experimental phase distribution is not presented.

V. ANALYSIS OF THE SCATTERING EFFICIENCY

Next, we investigate the performance of the structure, operating as a scatterer in free space [the configuration in Fig. 2(c)]. The optical theorem is used to evaluate the total scattering efficiency from the imaginary part of the forward one in the case of the experimental acquisition [43,44]. Experimental and numerical results are summarized in Fig. 6(a).

TABLE I. Characterization of the resonant modes, experimental, and numerical data. Modes are characterized by their azimuthal order, dominating multipole, resonant frequency, and quality factor. Cartesian multipoles: ED and MD, electric and magnetic dipoles; EQ and MQ, electric and magnetic quadrupoles; EO and MO, electric and magnetic octupoles; M16-pole, magnetic hexadecapole; M32-pole, magnetic triakontadipole.

	Experimental data							
Azimuthal order	0	1	2	3	4	4	5	5
f, GHz	–	–	2.055	2.181	2.23	2.239	2.253	2.258
Q factor	–	–	32.5	220	1316	1595	1211	2579
	Numerical data							
Contributing multipoles	ED	MD+EQ	MQ+EO	MO	M16-pole	M16-pole	M32-pole	M32-pole
f, GHz	1.773	1.887	2.094	2.217	2.273		2.295	
Q factor	1.1	3.8	20	120	873		5599	

While the experimental data is colored by an additional oscillatory pattern, which is quite similar to experiments, performed in an anechoic chamber (e.g., Refs. [45,46]), a good correspondence with the numerical data can be observed. Main high-Q peaks are clearly visible, and their spectral positions are predicted by the numerical modeling (a 40-MHz shift was manually compensated to obtain more accurate layout of the results). It is also worth noting the similarity between Figs. 5 and 6(a), despite different experimental layouts, used to obtain the data. This is the manifestation of strong resonant behavior, which predominates other mechanisms (e.g., absorption) that might play a role. High-Q modes are the preferable channels for radiation and scattering; hence, they are visible in both cases (Figs. 5 and 6). It is worth clarifying that far-to-far field excitation characterizes the structure in terms of scattering efficiency as a passive device, whereas near-to-far field excitation allowed for probing its modes.

In order to reveal the contribution of eigenmodes to the scattering performance, we perform the decomposition of the simulated scattered field with respect to Cartesian multipoles
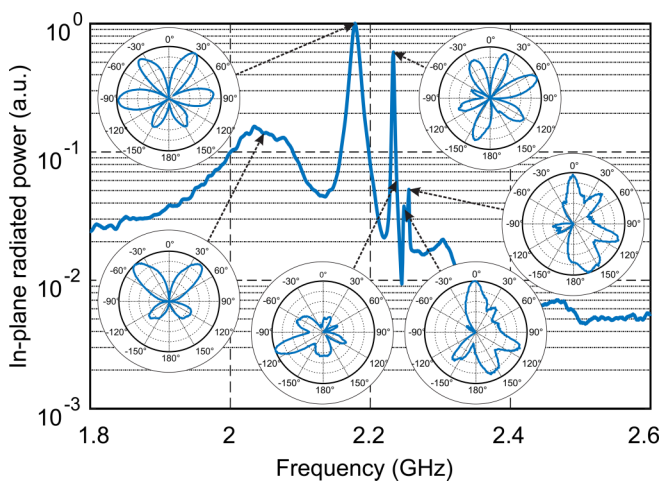

FIG. 5. In-plane radiated power as a function of frequency. Insets; radiation patterns (E field), the setup from Fig. 2(b). Frequencies correspond to resonant modes, which appear in Table I. Radiation patterns are normalized to the maxima.
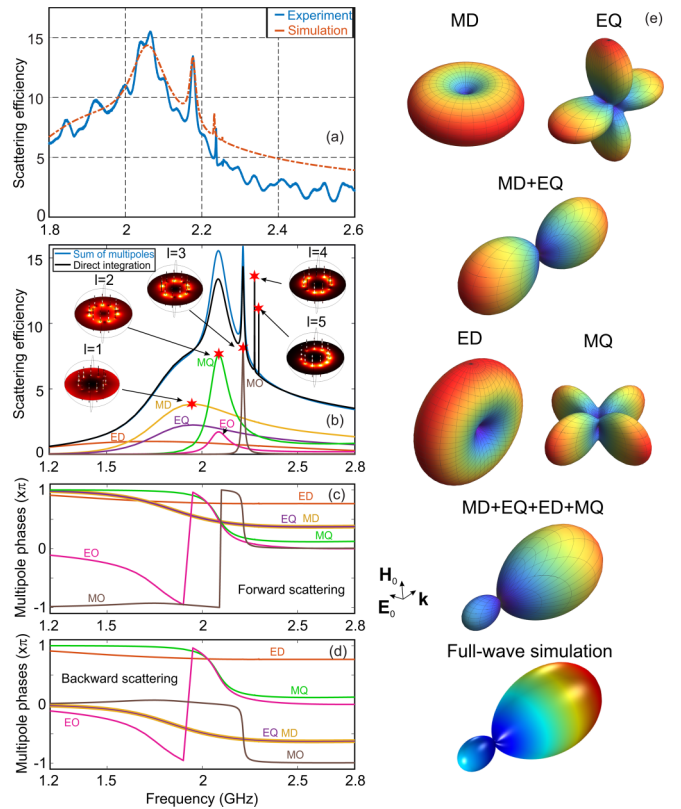

FIG. 6. Scattering efficiency analysis. (a) Measured and simulated scattering efficiencies spectra. (b) Cartesian multipole decomposition of the scattering efficiency. Multipole contributions are marked with colors: ED and MD, electric and magnetic dipoles; EQ and MQ, electric and magnetic quadrupoles; EO and MO, electric and magnetic octupoles. Blue line indicates summation of the multipolar contributions, while black line stands for the direct far-field integration. Insets show near-field distribution of the magnetic field in the equatorial plane and current distribution on the wires (white cones) at the eigenmode frequencies. Both figures correspond to the experimental layout in Fig. 2(c). Phases of multipole contributions to the far field in the (c) forward and (d) backward directions with respect to the wave incidence. EQ and MD are in-phase across the full frequency range. (e) Far-field scattering patterns for isolated multipoles, their sums, and full-wave simulation at 1.96 GHz. Orientation of the incident plane wave is equal for all patterns.

with three orders included as follows [40]:

$$E_{\text{scat}\_i} = \frac{k^2}{4\pi\varepsilon_0 r} e^{ikr}\Bigg[(n_i n_j - n^2\delta_{ij})\Bigg(-\bigg(p_j + \frac{ik}{c}T_j^{(e)} + \frac{ik^3}{c}T_j^{(2e)}\bigg) + \frac{ik}{2}\bigg(\bar{\bar{Q}}_{jk}^{(e)} + \frac{ik}{c}\bar{\bar{T}}_{jk}^{(Qe)}\bigg)n_k$$

$$+ \frac{k^2}{6}\bigg(\bar{\bar{O}}_{jkp}^{(e)} + \frac{ik}{c}\bar{\bar{T}}_{jkp}^{(Oe)}\bigg)n_k n_p\Bigg) + \varepsilon_{ikj}n_k\bigg(-\frac{1}{c}\bigg(m_j + \frac{ik}{c}T_j^{(m)}\bigg) + \frac{ik}{2c}\bigg(\bar{\bar{Q}}_{jp}^{(m)} + \frac{ik}{c}\bar{\bar{T}}_{jp}^{(Qm)}\bigg)n_p + \frac{k^2}{6c}\bar{\bar{O}}_{jpl}^{(m)}n_p n_l\bigg)\Bigg]$$

We assume $\exp(-i\omega t)$ time dependence and Einstein's summation notation, where vectors and tensors are denoted by lower-case indexes. The following parameters are defined: k is the vacuum wave number, $r = |\mathbf{r}|$ the distance between the scatterer's center and the observation point, ε_0 is the vacuum permittivity, $n_i = r_i/r$; p_j and m_j are the basic ED and MD, $\bar{\bar{Q}}_{jk}^{(e)}$ and $\bar{\bar{Q}}_{jk}^{(m)}$ are the EQs and MQs, $\bar{\bar{O}}_{jkp}^{(e)}$ and $\bar{\bar{O}}_{jpl}^{(m)}$ are the EOs and MOs. The toroidal moments are marked with T. The superscripts in round brackets indicate their belonging to the corresponding basic multipole moments. Explicit expressions for multipole tensors can be found in Ref. [40]. The differential scattering power is given by

$$dP_{\text{scat}} = \frac{1}{2}\sqrt{\frac{\varepsilon_0}{\mu_0}}|\mathbf{E}_{\text{scat}}|^2 d\Omega.$$

Normalization of P_{scat} to the incident wave energy flux and the geometrical efficiency of the scatterer leads to the following expression for the scattering efficiency:

$$\sigma_{\text{scat}} = \frac{2}{2RL}\sqrt{\frac{\mu_0}{\varepsilon_0}}\frac{P_{\text{scat}}}{|\mathbf{E}_0|^2},$$

where $|\mathbf{E}_0|$ is the amplitude of the incident field.

Figure 6(b) summarizes the results. The validity of the decomposition is evidenced from the agreement between the sum of multipole contributions and the scattering efficiency obtained by the integration of scattered field. The only significant differences appear for the highest order modes with $l = 4$ and $l = 5$ because the order of multipoles to which they correspond is beyond the set of six considered multipoles. However, accounting for the symmetry of these modes, one can assume that the dominating multipoles for in this case are M16- and M32-poles, respectively.

It is important to note that magnetic multipoles prevail over electric counterparts for all eigenmodes except for the lowest order ED mode. This is the result of alternating wire polarizations serving as sources of magnetic field which is shown in the insets of Fig. 6(b) and confirmed by the phase patterns, presented in Fig. 4.

VI. BROADBAND HUYGENS ELEMENT

The broadband performance of the system is mainly provided by the zero-, first-, and second-order azimuthal modes, which contain ED, MD+EQ, and MQ+EO multipoles, respectively [Fig. 6(b)]. Hence, the behavior of the scattering pattern in the broadband frequency domain is determined by the interference between these multipoles. Figures 6(c) and 6(d) show an analysis of the far-field phases for the multipole contributions. We distinguish phases for the forward and backward directions with respect to the incident plane

wave. Interestingly, couples of multipoles contributing to the same eigenmodes MD + EQ and MQ+EO are in-phase in both directions in the spectral ranges of mode existence. Moreover, the strength of particular multipole contributions to the scattering correlates well with their constructive and destructive interference in the forward and backward directions, respectively. For example, at the frequencies less than 2 GHz the major contributing multipoles are ED, MD, EQ, and MQ [Fig. 6(b)]. The phase shift between them in the forward direction is much less than π [Fig. 6(c)], and ED and MQ are shifted approximately by π from MD and EQ in the backward direction [Fig. 6(d)]. The same situation appears for other combinations of major contributing multipoles in other frequency ranges. Hence, the broadband forward scattering pattern is formed.

It is also instructive to analyze this generalized Kerker effect at the level of scattering patterns. Figure 6(e) demonstrates far-field scattering patterns for isolated multipoles and their sums at the eigenfrequency of the first-order azimuthal mode 1.96 GHz. The sum of MD and EQ (which form the first-order azimuthal mode) results in the equal scattering in the forward and backward directions, which follows from the analysis of the multipole phases as well. However, accounting for ED and MQ gives rise to the pronounced forward scattering, as confirmed by the full-wave simulation.

Next, we compare the forward and the backward scattering efficiencies predicted by the theoretical model with the measurements (Fig. 7). Once the forward-to-backward ratio prevails the value of 2 (rather arbitrary yet reasonable criteria), the element can be considered as Huygens. One can observe a minimum of the backward scattering at 1.93 GHz in the experiment [Fig. 7(a)] and at 1.6 GHz in the simulation [Fig. 7(b)], which corresponds to the maximum in the forward-to-backward ratio (frequency shift between the numerical and experimental results are quite common and may be as large as 10% of the carrier in the case resonant structures are in use). This is the result of the classical Kerker effect [24] associated with almost equal and in-phase ED, MD, and EQ contributions to the scattering [Figs. 6(b)–6(d)]. At higher frequencies, the directional resonant scattering is achieved over a relatively broad spectral range, covering 10s of percent of the bandwidth [Figs. 7(c) and 7(d)] for the experiment and the theory). Scattering patterns, which appear as insets in Fig. 7(d), clearly show dominating forward scattering. The only exceptions are the fourth- and fifth-order azimuthal modes that impinge the forward scattering due to the very multilobe structures. Nevertheless, apart from several spectral notches the generalized Kerker effect is supported in the rest part of the spectrum. It should be noted that the effect here is different from other broadband Huygens elements, based on nonresonant elements [30,32]. In nonresonant cases the
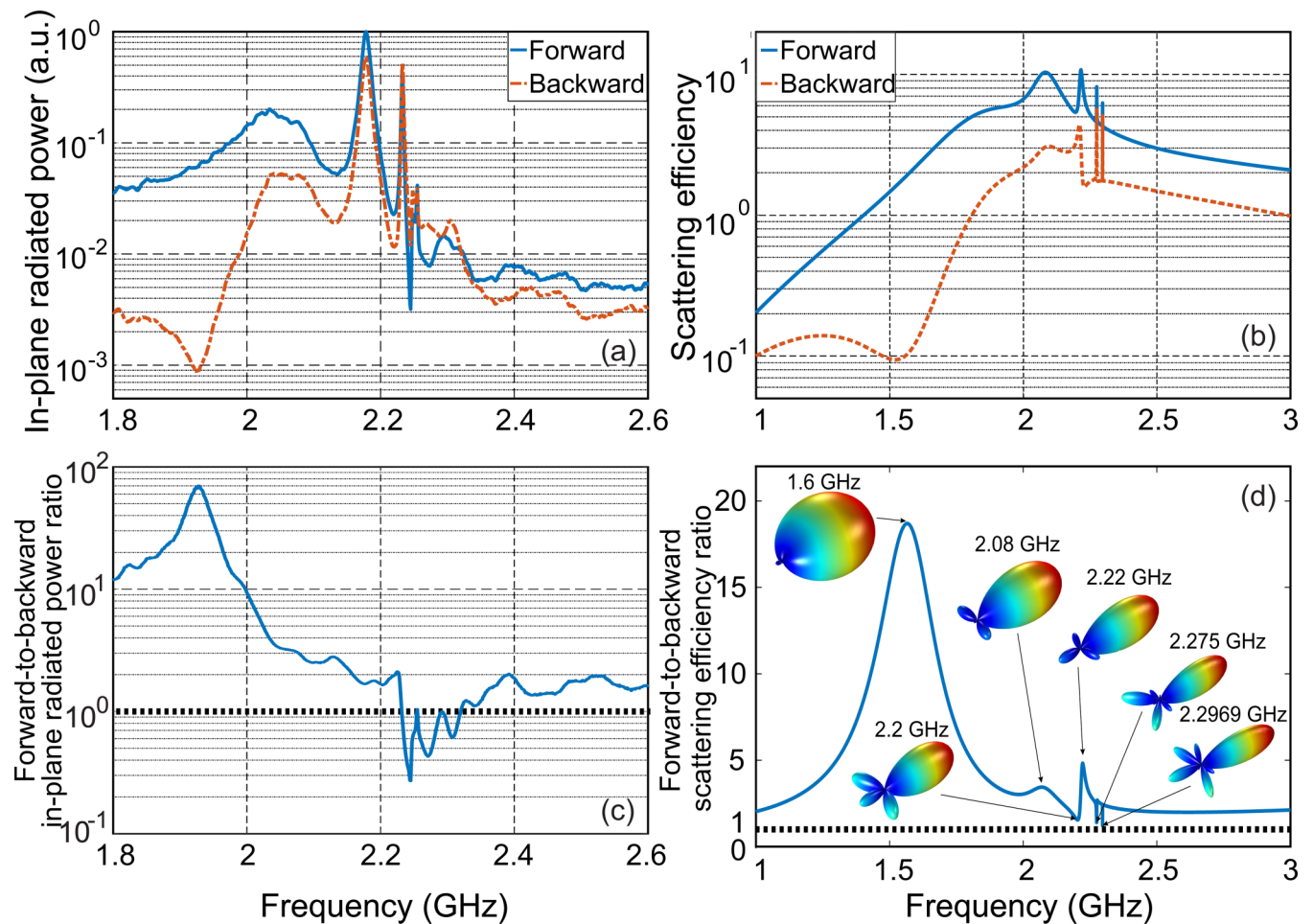
FIG. 7. Forward and the backward scattering efficiency spectra: (a) experimental, (b) numerical. Forward-to-backward scattering ratio: (c) experimental, (d) numerical. Insets: far-field scattering diagrams. Measurements have been performed for two directions only, while in simulations the forward and backward scattering efficiencies have been calculated by integrations of the far-field over hemispheres.

scattering efficiencies are much weaker and spectral control over the effect is more challenging if even possible.

VII. CONCLUSION AND OUTLOOK

The concept of a broadband resonant Huygens element based on a circular array of vertically aligned metal wires has been proposed and experimentally demonstrated. The effect stems from spectral cascading a variety of system's eigenmodes appearing as a result of a strong near-field coupling between dipolar responses of individual wires. Field expansion with respect to Cartesian multipoles shows predominant contribution of magnetic multipoles with respect to electric ones for almost all eigenmodes except from the lowest one. Very high-order magnetic hexadecapole (M16-pole) and magnetic triakontadipole (M32-pole) with quality factors, approaching 6000, have been predicted and mapped with a near-field scanner. Multipoles contribution to the Huygens element performance have been shown. Scattering efficiency of the demonstrated configuration is 15 times larger than its geometrical cross section and, at the same time, the device demonstrates broadband forward scattering capabilities,

obtained at a bandwidth ∼10% of the carrier frequency in the GHz range.

Resonant Huygens elements of this kind can find a use in frequency-selective surfaces designs, antenna isolation devices, directional reflectors, refractors, and many others. It is also worth noting that the concept can be scaled in frequency and the resonant cascading approach can be mapped on the optical domain, taking into account corresponding issues of material losses and dispersion, which are not the scalable quantities. Resonant cascading in optics is valuable for light harvesting, which is an important objective, contributing to green energy efforts and flat miniaturized imaging optics to name just few. For example, Huygens metasurfaces are used for implementing flat objectives with high numerical apertures [47] and in other all-dielectric photonic applications [14].

[1] R. F. Harrington, *Time-Harmonic Electromagnetic Fields*, 2nd ed. (Wiley-IEEE Press, New York, 2001).

[2] B. S. Luk'yanchuk, M. I. Tribelsky, V. Ternovsky, Z. B. Wang, M. H. Hong, L. P. Shi, and T. C. Chong, J. Opt. A **89**, 294 (2007).

[3] M. Born and E. Wolf, *Principles of Optics* (Cambridge University Press, Cambridge, 1999).

[4] C. F. Bohren and D. R. Huffman, *Absorption and Scattering of Light by Small Particles* (Wiley, New York, 1998).

[5] H. C. van de Hulst, *Light Scattering by Small Particles* (Dover, New York, 1981).

[6] D. Filonov, A. Shmidt, A. Boag, and P. Ginzburg, Appl. Phys. Lett. **113**, 123505 (2018).

[7] D. Margetis, G. Fikioris, J. M. Myers, and T. T. Wu, Phys. Rev. E **58**, 2531 (1998).

[8] Z. Ruan and S. Fan, Phys. Rev. Lett. **105**, 013901 (2010).

[9] Z. Ruan and S. Fan, Appl. Phys. Lett. **98**, 043101 (2011).

[10] I. Liberal, I. Ederra, R. Gonzalo, and R. W. Ziolkowski, J. Opt. **17**, 072001 (2015).

[11] R. W. Ziolkowski, Phys. Rev. X **7**, 031017 (2017).

[12] I. Sushencev, A. A. Shcherbakov, K. Ladutenko, and P. Belov, in *2019 IEEE International Conference on Microwaves, Communications, Antennas, and Electronic Systems* (IEEE, New York, 2019), pp. 1–3.

[13] R. C. Hansen and John Wiley & Sons, *Electrically Small, Superdirective, and Superconducting Antennas* (Wiley-Interscience, New York, 2006).

[14] A. I. Kuznetsov, A. E. Miroshnichenko, M. L. Brongersma, Y. S. Kivshar, and B. Luk'yanchuk, Science **354**, aag2472 (2016).

[15] A. V. Kildishev, A. Boltasseva, and V. M. Shalaev, Science **339**, 1232009 (2013).

[16] N. Yu and F. Capasso, Nat. Mater. **13**, 139 (2014).

[17] D. Lin, P. Fan, E. Hasman, and M. L. Brongersma, Science **345**, 298 (2014).

[18] L. Shao, W. Zhu, M. Y. Leonov, and I. D. Rukhlenko, J. Appl. Phys. **125**, 203101 (2019).

[19] J. Zhang, X. Wei, I. D. Rukhlenko, H.-T. Chen, and W. Zhu, ACS Photonics **7**, 265 (2020).

[20] M. R. Akram, M. Q. Mehmood, T. Tauqeer, A. S. Rana, I. D. Rukhlenko, and W. Zhu, Opt. Express **27**, 9467 (2019).

[21] R. E. Noskov, A. A. Zharov, and M. V. Tsarev, Phys. Rev. B **82**, 073404 (2010).

[22] R. E. Noskov, D. A. Smirnova, and Y. S. Kivshar, Philos. Trans. R. Soc. A **372**, 20140010 (2014).

[23] J. Xie, S. Quader, F. Xiao, C. He, X. Liang, J. Geng, R. Jin, W. Zhu, and I. D. Rukhlenko, IEEE Antennas Wirel. Propag. Lett. **18**, 536 (2019).

[24] M. Kerker, D.-S. Wang, and C. L. Giles, J. Opt. Soc. Am. **73**, 765 (1983).

[25] J. M. Geffrin, B. García-Cámara, R. Gómez-Medina, P. Albella, L. S. Froufe-Pérez, C. Eyraud, A. Litman, R. Vaillon, F. González, M. Nieto-Vesperinas, J. J. Sáenz, and F. Moreno, Nat. Commun. **3**, 1171 (2012).

[26] A. E. Krasnok, A. E. Miroshnichenko, P. A. Belov, and Y. S. Kivshar, JETP Lett. **94**, 593 (2011).

[27] H. K. Shamkhi, K. V. Baryshnikova, A. Sayanskiy, P. Kapitanova, P. D. Terekhov, P. Belov, A. Karabchevsky, A. B. Evlyukhin, Y. Kivshar, and A. S. Shalin, Phys. Rev. Lett. **122**, 193905 (2019).

[28] V. Kozlov, D. Filonov, A. S. Shalin, B. Z. Steinberg, and P. Ginzburg, Appl. Phys. Lett. **109**, 203503 (2016).

[29] D. Filonov, V. Kozlov, A. Shmidt, B. Z. Steinberg, and P. Ginzburg, Appl. Phys. Lett. **113**, 094103 (2018).

[30] H. Barhom, A. A. Machnev, R. E. Noskov, A. Goncharenko, E. A. Gurvitz, A. S. Timin, V. A. Shkoldin, S. V. Koniakhin, O. Y. Koval, M. V. Zyuzin, A. S. Shalin, I. I. Shishkin, and P. Ginzburg, Nano Lett. **19**, 7062 (2019).

[31] W. Liu and Y. S. Kivshar, Opt. Express **26**, 13085 (2018).

[32] M. I. Abdelrahman, H. Saleh, I. Fernandez-Corbaton, B. Gralak, J.-M. Geffrin, and C. Rockstuhl, APL Photon. **4**, 020802 (2019).

[33] R. E. Collin and F. J. Zucker, *Antenna Theory* (McGraw-Hill, New York, 1969).

[34] H. M. Aumann, in *2008 IEEE Int. Symp. Antennas Propag. Usn. Natl. Radio Sci. Meet. APSURSI* (CA, San Diego, 2008).

[35] R. W. P. King, G. J. Fikioris, and R. B. Mack, *Cylindrical Antennas and Arrays* (Cambridge University Press, Cambridge, 2002).

[36] G. Fikioris, S. Lygkouris, and P. J. Papakanellos, IEEE Trans. Antennas Propag. **59**, 4615 (2011).

[37] G. Fikioris, S. D. Zaharopoulos, and P. D. Apostolidis, IEEE Trans. Antennas Propag. **53**, 3906 (2005).

[38] L. Josefsson and P. Persson, *Conformal Array Antenna Theory and Design* (Wiley, Hoboken, NJ, 2006).

[39] P. Nordlander, C. Oubre, E. Prodan, K. Li, and M. I. Stockman, Nano Lett. **4**, 899 (2004).

[40] E. A. Gurvitz, K. S. Ladutenko, P. A. Dergachev, A. B. Evlyukhin, A. E. Miroshnichenko, and A. S. Shalin, Laser Photon. Rev. **13**, 1800266 (2019).

[41] M. Hentschel, M. Saliba, R. Vogelgesang, H. Giessen, A. P. Alivisatos, and N. Liu, Nano Lett. **10**, 2721 (2010).

[42] A. Alù, A. Salandrino, and N. Engheta, Opt. Express **14**, 1557 (2006).

[43] M. Born and E. Wolf, *Principles of Optics: Electromagnetic Theory of Propagation, Interference and Diffraction of Light*, 7th ed. (Cambridge University Press, Cambridge, 1999).

[44] A. V. Krasavin, P. Segovia, R. Dubrovka, N. Olivier, G. A. Wurtz, P. Ginzburg, and A. V. Zayats, Light Sci. Appl. **7**, 36 (2018).

[45] H. Markovich, D. Filonov, I. Shishkin, and P. Ginzburg, IEEE Trans. Antennas Propag. **66**, 2650 (2018).

[46] D. S. Filonov, A. S. Shalin, I. Iorsh, P. A. Belov, and P. Ginzburg, J. Opt. Soc. Am. A **33**, 1910 (2016).

[47] R. Paniagua-Domínguez, Y. F. Yu, E. Khaidarov, S. Choi, V. Leong, R. M. Bakker, X. Liang, Y. H. Fu, V. Valuckas, L. A. Krivitsky, and A. I. Kuznetsov, Nano Lett. **18**, 2124 (2018).